Journal of Computational Physics 229 (2010) 2719–2739

Contents lists available at ScienceDirect

Journal of Computational Physics

journal homepage: www.elsevier.com/locate/jcp

Second order front tracking for the Euler equations

Jeroen A.S. Witteveen *

Center for Turbulence Research, Stanford University, Building 500, Stanford, CA 94305-3035, USA

ARTICLE INFO

Article history:
Received 17 August 2009
Received in revised form 20 November 2009
Accepted 14 December 2009
Available online 29 December 2009

Keywords:
Hyperbolic conservation laws
Piecewise linear approximation
Riemann problem
Blast waves problem
Supersonic airfoil flow

ABSTRACT

A second order front tracking method is developed for solving the hyperbolic system of Euler equations of inviscid fluid dynamics numerically. Meshless front tracking methods are usually limited to first order accuracy, since they are based on a piecewise constant approximation of the solution. Here second order convergence is achieved by deriving a piecewise linear reconstruction of the piecewise constant front tracking solution. The linearization is performed by decomposing the front tracking solution into its wave components and by linearizing the wave solutions separately. In order to construct a physically correct linearization, the physical phenomena of the front are taken into account in terms of the front types of the previously developed improved front interaction model. This front interaction model is also extended to include front numbers used in the wave decomposition. It is illustrated numerically for Sod's Riemann problem, the two interacting blast waves problem, and a two-dimensional supersonic airfoil flow validation study that the proposed front tracking method achieves second order convergence also in the presence of strong discontinuities and their interactions.

1. Introduction

Front tracking is known to be an effective tool for resolving discontinuities in the solution of hyperbolic conservation laws. One type of front tracking methods initiated by Richtmyer and Morton [23] uses a fixed background mesh to solve for continuous phenomena and introduces additional degrees of freedom to model discontinuities such as shock waves and two fluid interfaces. This branch of front tracking has since then been extended to resolve complex instabilities and bifurcations by Moretti [16], Swartz and Wendroff [28], and Chern, Glimm, and coworkers [4,9–11]. This includes wave labeling techniques and the combination with second order finite volume discretizations on the background mesh [3]. A theoretical study on this type of front tracking is presented in [6] and in [5,12] conservative front tracking methods are considered.

A second type of meshless front tracking methods exists that resolves both the discontinuities and the continuous regions of the solution domain [15]. Meshless front tracking introduced by Risebro and Tveito [25] does not require a background mesh by approximating continuous phenomena using a series of small discontinuities. This class of front tracking methods has been used as an analytical tool for studying scalar equations and systems of hyperbolic conservation laws [1,2]. It has also been employed as a numerical scheme to solve one-dimensional problems in shallow water flows [13], gas dynamics [18], and polymer flooding [24]. One-dimensional front tracking is of interest in, for example, pipe flows and shock tube problems. An equivalent algorithm can also be used to simulate two-dimensional supersonic flows [31]. Meshless front tracking has been extended to higher dimensions using dimensional splitting techniques by Holden, Lie, et al. [14,19].

* Tel.: +1 650 723 9601; fax: +1 650 723 9617.
E-mail address: jeroenwitteveen@stanford.edu

0021-9991/$ - see front matter © 2009 Elsevier Inc. All rights reserved.
doi:10.1016/j.jcp.2009.12.019

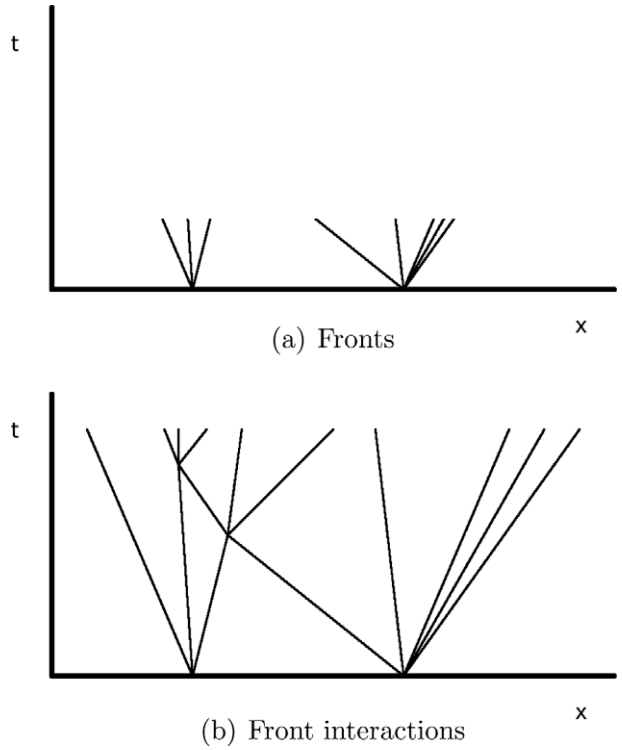

Fig. 1. Front tracking discretization in space–time.

Here the branch of meshless front tracking methods is considered as a numerical approach for solving the hyperbolic Euler equations of inviscid fluid dynamics. The numerical algorithm is based on a piecewise constant approximation of the solution of local Riemann problems. The first step in the solution procedure for an initial value problem is the piecewise constant approximation of the initial conditions. At the discontinuities in this discretization the flow conditions resemble the initial conditions of a local Riemann problem. The piecewise constant approximation of the solution of these Riemann problems results in the introduction of new discontinuities which move in time. The paths of these discontinuities are tracked by fronts in the space–time domain, see Fig. 1. In nonlinear problems the front velocities are in general different for different fronts, such that they can intersect at a later time. At an intersection point the discontinuous solution is locally again equal to the initial conditions of a Riemann problem. The piecewise constant approximation of the solution of this Riemann problem results in the introduction of more fronts which can again intersect with other fronts and so on, until a certain time $t = \bar{t}$ is reached.

Recently an improved front interaction model was proposed to obtain a physically more accurate simulation of the front interactions for the Euler equations [31]. In the improved model the physical phenomena of the fronts are explicitly taken into account to predict the wave pattern that is created at an intersection point based on gas dynamics theory. To that end, front types are assigned to the fronts to track the wave phenomena that the fronts represent. This information is then used in a modified Riemann solver, instead of solving a standard Riemann problem in the intersection points.

The piecewise constant front tracking solution is effective for resolving shock waves and contact discontinuities as true discontinuities. In that sense the method contains no artificial numerical viscosity and it can be considered an unconditionally stable scheme [14]. However, due to the piecewise constant approximation of the solution, front tracking methods usually result in first order error convergence [15]. It has been illustrated numerically that integral quantities are approximated with second order accuracy for the conservation of mass, momentum, and energy [31], and the location of the fronts [30]. Second order convergence for a scalar conservation law in one dimension was proven by Lucier [21] for a piecewise linear approximation through nodes moving according to the method of characteristics.

In this paper, a second order front tracking method for the system of Euler equations is proposed by using the front types of the improved front interaction model. The second order accurate solution is obtained by a piecewise linear reconstruction of the piecewise constant front tracking solution. In contrast to scalar equations, systems of conservation laws allow for multiple waves to coexist in any location in the space–time domain. The piecewise linear approximation is, therefore, constructed by decomposing the front tracking solution into a series of wave solutions and by linearizing the wave components separately. The piecewise linear front tracking solution is finally obtained by summing the linearized wave solutions. This approach is based on the observation that, although the nonlinear problem itself cannot be *solved* by summing

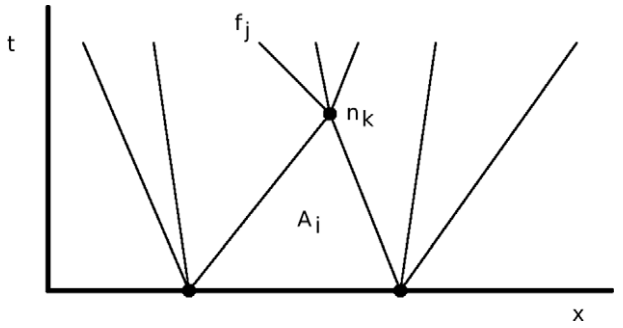

Fig. 2. Front tracking notation in space–time.

wave solutions, the nonlinear front tracking solution can nonetheless be *decomposed* into a summation of wave components. In order to obtain a physically consistent linearization the front types of the improved front interaction model are employed.

In contrast to the earlier first order improved front tracking method [31] the current work presents a front tracking method which reaches a second order convergence rate. To enable the second order piecewise linear reconstruction, front numbers and a front number interaction model are introduced into the formulation. The application of the method to two-dimensional supersonic airfoil flow is also extended to non-zero angles of attack using a domain decomposition approach.

The piecewise linear front tracking method is introduced in Section 3 after a brief review of the standard and improved meshless front tracking methods in Section 2. In Sections 4 and 5 the properties of the developed method are analyzed in application to Sod's Riemann problem and the two interacting blast waves problem, respectively. The results are compared with the first order front tracking method and a second order Godunov finite volume scheme. Results for a two-dimensional supersonic airfoil flow problem are validated with respect to experimental PIV velocity measurements in Section 6. The paper is concluded in Section 7.

2. Front tracking for the Euler equations

Meshless front tracking for the Euler equations is described in Section 2.1. In Section 2.2 the formulation of the improved front interaction model is revisited in more detail, since its front types are used in the linearization algorithm.

2.1. Meshless front tracking

The Euler equations for one-dimensional unsteady inviscid flow without heat conduction are given in conservation form by

$$\frac{\partial U}{\partial t}+\frac{\partial F(U)}{\partial x}=0, \tag{1}$$

where

$$U=\begin{pmatrix}\rho\\ \rho u\\ \rho E\end{pmatrix},\quad F=\begin{pmatrix}\rho u\\ \rho u^2+p\\ \rho u H\end{pmatrix},\quad U(x,0)=U_0(x), \tag{2}$$

with state vector $U(x,t)$, flux vector $F(x,t)$, and initial condition $U_0(x)$ in terms of density $\rho(x,t)$, velocity $u(x,t)$, static pressure $p(x,t)$, total energy $E(x,t)$, and enthalpy $H(x,t)$ as function of spatial coordinate $x\in\mathbb{R}$ and time $t\in\mathbb{R}^+$, see for example [7]. A perfect gas is considered for which holds $E=(1/(\gamma-1))p/\rho+u^2/2$ and $H=E+p/\rho$, with ratio of specific heats $\gamma=c_p/c_v$.

A front tracking method approximates the solution of (1) in the space–time plane by a piecewise constant function based on uniform flow conditions U_i in n_{cell} cells A_i with $i=1,\ldots,n_{\text{cell}}$, see Fig. 2. The cell boundaries are composed of n_{front} linear front paths f_j with $j=1,\ldots,n_{\text{front}}$, where the fronts follow physical wave phenomena, such as shock waves, contact waves, and characteristics. The starting and end points of the front paths f_j form a set of n_{node} nodes $n_k=(x_{n_k},t_{n_k})$ in space–time with $k=1,\ldots,n_{\text{node}}$. Pointers are used to establish the relation between cells A_i and fronts f_j, and fronts f_j and nodes n_k.

In the first step of the front tracking algorithm the piecewise constant approximation of the initial conditions $U_0(x)$ results in the introduction of n_{node_0} nodes n_k with $t_{n_k}=0$ for $k=1,\ldots,n_{\text{node}_0}$ at the discontinuities in the discretized initial conditions. At the nodes n_k the flow conditions resemble locally the initial conditions of a Riemann problem given by

$$U_0(x)=\begin{cases}U^-, & x_{n_k}<0,\\ U^+, & x_{n_k}\geqslant 0,\end{cases} \tag{3}$$

for $k = 1, \ldots, n_{\text{node}_0}$, with U^- and U^+ the constant left and right states of node n_k, respectively. The piecewise constant approximation of the solution of the n_{node_0} Riemann problems leads to the creation of n_{front_0} fronts f_j with constant front velocities u_{front_j} emanating from the nodes with $j = 1, \ldots, n_{\text{front}_0}$. At the first intersection of fronts at $t = t_1$ a new node n_k with $k = n_{\text{node}_0} + 1$ and $t_{n_k} = t_1 z$ is created and a Riemann problem is solved, and so forth until $t = \tilde{t}$.

The accuracy of the simulation is mainly governed by the number of nodes used in the discretization of continuous initial and boundary conditions, and the number of fronts n_f that is used to discretize centered rarefaction fans. The number of fronts n_f can be determined adaptively based on the strength of the rarefaction fan by a user defined discretization parameter δ

$$n_f = \max\left\{2, \left\lceil \frac{\Delta_{\text{crw}}}{\delta} \right\rceil \right\}, \tag{4}$$

with Δ_{crw} the strength of the centered rarefaction wave (crw) defined as

$$\Delta_{\text{crw}} = \frac{1}{3}\left(\frac{|u_l - u_r|}{\frac{1}{2}(|u_l| + |u_r|)} + \frac{|p_l - p_r|}{\frac{1}{2}(|p_l| + |p_r|)} + \frac{|\rho_l - \rho_r|}{\frac{1}{2}(|\rho_l| + |\rho_r|)} \right), \tag{5}$$

where subscripts l and r denote the left and right state of the wave, respectively. The stop criterion for the iterative solution of the Riemann problems also affects the simulation accuracy. The Riemann solver used here is based on an iteration of analytical isentropic Riemann solutions comparable to the one described in [8]. The resulting piecewise constant front tracking solution converges with first order accuracy [15]. Usually only interactions of two fronts are considered without loss of generality [1]. The build up of the number of fronts n_{front} is controlled by disregarding weak fronts. To that end the strength of each front Δ_{front_j} is described in analogy to (5) for centered rarefaction fans, where the subscripts l and r refer in this case to the left and right state of the front. A cut-off criterion δ_{front} is prescribed to eliminate weak fronts for which holds

$$\Delta_{\text{front}_j} < \delta_{\text{front}}, \tag{6}$$

from the discretized solution of the Riemann problem. The left and right state of the neglected front are then averaged.

2.2. Improved front interaction model

In the improved front tracking method for the Euler equations [31] a better physical modeling of the front interactions is obtained by explicitly taking into account the wave phenomena that the fronts represent. The following front types f_{type_j} are used to track the wave phenomena of the fronts

$$f_{\text{type}_j} \in \{\text{sw}, \text{lch}, \text{ich}, \text{rch}, \text{cd}, \text{lcw}, \text{icw}, \text{rcw}\}, \tag{7}$$

for $j = 1, \ldots, n_{\text{front}}$. The front types distinguish between shock waves (sw), left/internal/right characteristics of a fan of characteristics (lch/ich/rch), contact discontinuities (cd), and left/internal/right contact waves discretizing a region of continuous change of entropy (lcw/icw/rcw). Also front families

$$f_{\text{family}_j} \in \{-, 0, +\}, \tag{8}$$

for $j = 1, \ldots, n_{\text{front}}$, are assigned to the fronts to denote left running (−), right running (+), and convective (0) fronts. The front type f_{type_j} and family f_{family_j} govern both the interaction with other fronts in the improved front interaction model and the relation for the front velocity u_{front_j} in terms of its left and right state. The interaction model prescribes the wave pattern originating from an intersection point in terms of the wave types

$$w_{\text{type}_l} \in \{\text{sw}, \text{lch}, \text{ich}, \text{rch}, \text{cd}, \text{lcw}, \text{icw}, \text{rcw}, \text{crw}\}, \tag{9}$$

with $l = \{\text{left}, \text{middle}, \text{right}\}$, of the created left, middle, and right waves w_l as function of f_{type_j} and f_{family_j} of the two intersecting fronts, j_{left} and j_{right}, see Fig. 3(a). Wave types w_{type_l} differ from front types f_{type_j} in the sense that the former include centered rarefaction waves (crw). A centered rarefaction wave is discretized by a series of fronts representing characteristics (lch/ich/rch). The model consists of three functions g_l for which holds

$$w_{\text{type}_l} = g_l(f_{\text{type}_{j_{\text{left}}}}, f_{\text{type}_{j_{\text{right}}}}, f_{\text{family}_{j_{\text{left}}}}, f_{\text{family}_{j_{\text{right}}}}), \tag{10}$$

for $l = \{\text{left}, \text{middle}, \text{right}\}$. The functions g_l are derived from theoretical gas dynamics [20] and are given in tabulated form in [31]. The front types f_{type_j} of the fronts created at the intersection point are then derived from the wave types w_{type_l} as follows

$$f_{\text{type}_j} \begin{cases} = w_{\text{type}_l}, & w_{\text{type}_l} \neq \text{crw}, \\ \in \{\text{lch}, \text{ich}, \text{rch}\}, & w_{\text{type}_l} = \text{crw}, \end{cases} \tag{11}$$

if front f_j is part of wave w_l. The front families f_{family_j} are determined by whether the front is created as part of the left, middle, or right wave of the solution of the Riemann problem

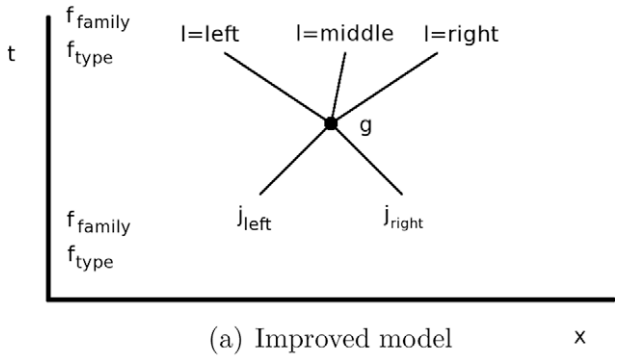

(a) Improved model

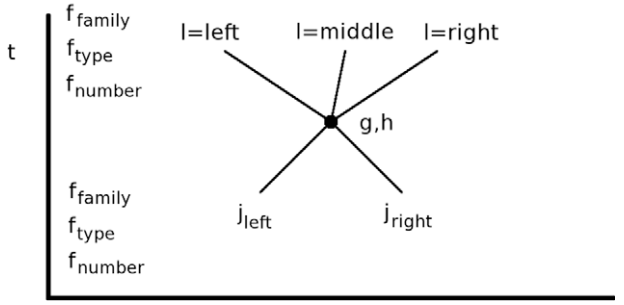

(b) Front number interaction model

Fig. 3. Front interaction models.

$$f_{\text{family}_j} = \begin{cases} -, & l = \text{left}, \\ 0, & l = \text{middle}, \\ +, & l = \text{right}, \end{cases} \tag{12}$$

with front f_j part of wave w_l. A non-standard Riemann solver, which takes into account whether the predicted wave types w_{type_l} are isentropic or possibly non-isentropic, is used to compute the post states U_i in the new cells and the velocities of the created fronts u_{front_j}. The front types f_{type_j} are also used in controlling the increase of the number of fronts with time by neglecting reflections of fronts that discretize continuous phenomena at front interactions with other continuous phenomena fronts (lch/ich/rch/lcw/icw/rcw).

The interaction of, for example, two centered rarefaction waves is in this framework resolved as follows. The rarefaction waves are first discretized by a series of small discontinuities using characteristic fronts (lch/ich/rch). The discrete interaction of the waves then results in a discontinuous change of the flow conditions at an intersection point of two of these fronts. Although the continuous problem does not involve a Riemann problem, the front interaction is resolved by solving an isentropic Riemann problem to take the isentropic nature of the reflected fronts into account. The Riemann problem is solved using one iteration of the Riemann solver, since the iterative Riemann solver is based on the analytical solution of the isentropic Riemann problem. This process is repeated for all intersections of the characteristic fronts.

3. Second order piecewise linear reconstruction

In addition to tracking the front types and front families, also wave numbers of the fronts need to be tracked for the piecewise linear reconstruction of the front tracking solution. The assignment of front numbers is considered in Section 3.1 in combination with the front interaction model for the front numbers. Tracking the wave numbers is necessary for the wave decomposition of the front tracking solution, described in Section 3.2, in order to linearize the wave solutions separately as discussed in Section 3.3. The last step of the algorithm summarized in Section 3.4 is the summation of the linearized wave solutions to obtain the piecewise linear front tracking solution.

3.1. Wave tracking

In order to perform the wave decomposition the n_{wave} waves in the front tracking solution in space–time are numbered using wave numbers ν_{number_m} with $m = 1, \ldots, n_{\text{wave}}$. To distinguish between these waves in space–time ν_m and the waves w_l

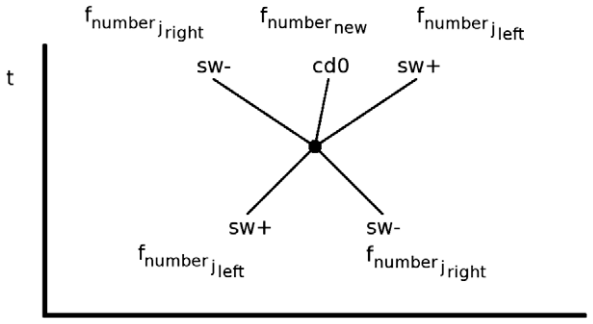

(a) Right and left running shock waves

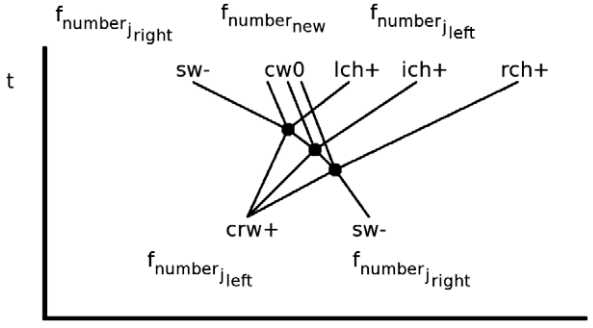

(b) Right running centered rarefaction wave and left running shock wave

Fig. 4. Front number interaction examples.

created at a front interaction a different notation is used for both cases. In this context a wave can be a shock wave, a fan of characteristics, a contact discontinuity, or a region of continuous change of entropy. To track which fronts belong to which wave, the wave numbers ν_{number_m} are assigned to the fronts in the form of front numbers f_{number_j} for which holds

$$f_{\text{number}_j} = \nu_{\text{number}_m}, \tag{13}$$

if front f_j is part of wave ν_m. In order to assign front numbers f_{number_j} to new fronts after a front intersection the interaction model has to be extended to prescribe also the wave numbers w_{number_l} of the created waves with $l = \{\text{left}, \text{middle}, \text{right}\}$. The wave numbers w_{number_l} are given by an additional front interaction function h_l which depends on the front types f_{type_j}, families f_{family_j}, and numbers f_{number_j} of the two intersecting fronts, j_{left} and j_{right},

$$w_{\text{number}_l} = h_l(f_{\text{type}_{j_{\text{left}}}}, f_{\text{type}_{j_{\text{right}}}}, f_{\text{family}_{j_{\text{left}}}}, f_{\text{family}_{j_{\text{right}}}}, f_{\text{number}_{j_{\text{left}}}}, f_{\text{number}_{j_{\text{right}}}}), \tag{14}$$

with $l = \{\text{left}, \text{middle}, \text{right}\}$, see Fig. 3(b). The function h_l can return the front number of one of the intersecting fronts or a new wave number

$$h_l \in \{f_{\text{number}_{j_{\text{left}}}}, f_{\text{number}_{j_{\text{right}}}}, \text{new wave number}\}, \tag{15}$$

for $l = \{\text{left}, \text{middle}, \text{right}\}$. The front number interaction function h_l is derived from gas dynamics theory in analogy to the improved front interaction model g_l and presented in tabulated form in Appendix A.

An example of the intersection of a right and left running shock wave, sw+ and sw−, is given in Fig. 4(a). It results in the continuation of the two shock waves and the creation of a contact discontinuity cd0. The front numbers f_{number_j} of the created left and right shock waves are equal to those of the intersecting right and left shock wave, j_{right} and j_{left}, respectively. The contact discontinuity has a new wave number.

If h_l prescribes that the created wave number is different from the wave numbers of the intersecting fronts, the number of waves is increased by one, $n_{\text{wave}} := n_{\text{wave}} + 1$, and the created wave is assigned the new wave number, $w_{\text{number}_l} = n_{\text{wave}}$. The number of the wave is then also assigned to the new fronts f_j which are part of the wave w_l according to

$$f_{\text{number}_j} = w_{\text{number}_l}. \tag{16}$$

In order to assign the new wave number to the entire wave and not only to its first created front, the relation between the created wave numbers w_{number_l} and the intersecting front numbers, $f_{\text{number}_{j\text{left}}}$ and $f_{\text{number}_{j\text{right}}}$, is stored in another tabulated function d_l with $l = \{\text{left}, \text{middle}, \text{right}\}$. At a later intersection of front numbers which are already tabulated in d_l, the created wave numbers are assigned according to table d_l

$$w_{\text{number}_l} = d_l(f_{\text{number}_{j_{\text{left}}}}, f_{\text{number}_{j_{\text{right}}}}), \tag{17}$$

for $l = \{\text{left}, \text{middle}, \text{right}\}$. If the intersecting front numbers $f_{\text{number}_{j_{\text{left}}}}$ and $f_{\text{number}_{j_{\text{right}}}}$ are not yet tabulated in d_l, then function h_l (14) is used to create the entry for the combination of $f_{\text{number}_{j_{\text{left}}}}$ and $f_{\text{number}_{j_{\text{right}}}}$ in d_l. In this way, for example, all contact waves cw0 created at the interaction of a right running centered rarefaction fan crw+ and a left running shock wave sw− are assigned the same new front number, see Fig. 4(b). Storing also the information of the front types f_{type_j} and families f_{family_j} of the intersecting fronts, j_{left} and j_{right}, in table d_l is not necessary.

3.2. Wave decomposition

The front numbers f_{number_j} are used to decompose the front tracking solution at $t = \tilde{t}$ into wave solutions. The piecewise constant solution $\widetilde{U}(x)$ in the $\tilde{n}_{\text{cell}}$ cells $\widetilde{A}_{\tilde{i}}$ at $t = \tilde{t}$ is denoted from left to right by $\widetilde{U}_{\tilde{i}}$ for $\tilde{i} = 1, \ldots, \tilde{n}_{\text{cell}}$. The tilde is used to differentiate between quantities at $t = \tilde{t}$ and those in space–time. The approximation is discontinuous at front locations $\tilde{x}_{\text{front}_{\tilde{j}}} = \tilde{x}_{\text{node}_{\tilde{k}}}$ for $\tilde{j} = 1, \ldots, \tilde{n}_{\text{front}}$, with $\tilde{j} = \tilde{k}$ and $\tilde{n}_{\text{front}} = \tilde{n}_{\text{node}}$. The $\tilde{n}_{\text{wave}}$ wave solutions present in the front tracking solution at $t = \tilde{t}$ are given by $\widetilde{V}_{\tilde{m}}(x)$ for $\tilde{m} = 1, \ldots, \tilde{n}_{\text{wave}}$ such that holds

$$\widetilde{U}(x) = \widetilde{U}_{\text{ref}} + \sum_{\tilde{m}=1}^{\tilde{n}_{\text{wave}}} \widetilde{V}_{\tilde{m}}(x), \tag{18}$$

where the reference value $\widetilde{U}_{\text{ref}} = \widetilde{U}(x_{\text{ref}})$ is chosen to be the value of $\widetilde{U}(x)$ in the leftmost point x_{ref} of the spatial domain, see Fig. 5(a). The wave solutions $\widetilde{V}_{\tilde{m}}(x)$ contain the $\tilde{n}_{\text{front}_{\tilde{m}}}$ fronts $\tilde{f}_{\tilde{m}_{\tilde{j}}}$ for which holds $\tilde{f}_{\text{number}_{\tilde{j}}} = \tilde{\nu}_{\text{number}_{\tilde{m}}}$ and the left and right boundary fronts. The piecewise constant wave solution $\widetilde{V}_{\tilde{m}}(x)$ is then given by

$$\widetilde{V}_{\tilde{m}}(x) = \widetilde{V}_{\tilde{m}_{\tilde{i}}}, \tag{19}$$

for $x \in \widetilde{A}_{\tilde{m}_{\tilde{i}}} = [\tilde{x}_{\text{front}_{\tilde{m}_{\tilde{j}}}}, \tilde{x}_{\text{front}_{\tilde{m}_{\tilde{j}+1}}}]$ with $\tilde{i} = \tilde{j}$ and

$$\widetilde{V}_{\tilde{m}_{\tilde{i}}} = \sum_{\tilde{j}=2}^{\tilde{i}} \widetilde{U}^{+}_{\tilde{m}_{\tilde{j}}} - \widetilde{U}^{-}_{\tilde{m}_{\tilde{j}}}, \tag{20}$$

with $\widetilde{U}^{-}_{\tilde{m}_{\tilde{j}}}$ and $\widetilde{U}^{+}_{\tilde{m}_{\tilde{j}}}$ the left and right states of front $\tilde{f}_{\tilde{m}_{\tilde{j}}}$, respectively, see Fig. 5(b) and (c). For the wave solutions $\widetilde{V}_{\tilde{m}}(x)$ holds that the solution in the first cell is $\widetilde{V}_{\tilde{m}_1} = 0$ for $\tilde{m} = 1, \ldots, \tilde{n}_{\text{wave}}$.

3.3. Piecewise linear reconstruction

The piecewise linear wave solutions $\widetilde{W}_{\tilde{m}}(x)$ are described by a linear variation in the cells $\widetilde{A}_{\tilde{m}_{\tilde{i}}}$

$$\widetilde{W}_{\tilde{m}}(x) = \widetilde{W}_{\tilde{m}_{\tilde{i}}}(x) = \frac{\widetilde{W}^{+}_{\tilde{m}_{\tilde{j}}}(\tilde{x}_{\text{front}_{\tilde{m}_{\tilde{j}+1}}} - x) + \widetilde{W}^{-}_{\tilde{m}_{\tilde{j}+1}}(x - \tilde{x}_{\text{front}_{\tilde{m}_{\tilde{j}}}})}{\tilde{x}_{\text{front}_{\tilde{m}_{\tilde{j}+1}}} - \tilde{x}_{\text{front}_{\tilde{m}_{\tilde{j}}}}}, \tag{21}$$

for $x \in \widetilde{A}_{\tilde{m}_{\tilde{i}}}$ and $\tilde{i} = \tilde{j}$, where $\widetilde{W}^{+}_{\tilde{m}_{\tilde{j}}}$ and $\widetilde{W}^{-}_{\tilde{m}_{\tilde{j}+1}}$ are the right and left states of the fronts $\tilde{f}_{\tilde{m}_{\tilde{j}}}$ and $\tilde{f}_{\tilde{m}_{\tilde{j}+1}}$ of the piecewise linear wave solution $\widetilde{W}_{\tilde{m}}(x)$, respectively. In determining the left and right states, $\widetilde{W}^{-}_{\tilde{m}_{\tilde{j}}}$ and $\widetilde{W}^{+}_{\tilde{m}_{\tilde{j}}}$, of the fronts $\tilde{f}_{\tilde{m}_{\tilde{j}}}$ the front types $\tilde{f}_{\text{type}_{\tilde{m}_{\tilde{j}}}}$ need to be taken into account, see Fig. 6(b) and (c). The linearization should not affect the approximation of discontinuous phenomena such as shock waves and contact discontinuities as true discontinuities. In that case the left and right states of the linearization are set to be equal to those of the piecewise constant wave solution

$$\widetilde{W}^{-}_{\tilde{m}_{\tilde{j}}} = \widetilde{V}^{-}_{\tilde{m}_{\tilde{j}}}, \qquad \widetilde{W}^{+}_{\tilde{m}_{\tilde{j}}} = \widetilde{V}^{+}_{\tilde{m}_{\tilde{j}}}, \tag{22}$$

if $\tilde{f}_{\text{type}_{\tilde{m}_{\tilde{j}}}} \in \{\text{sw}, \text{cd}\}$, with $\widetilde{V}^{-}_{\tilde{m}_{\tilde{j}}}$ and $\widetilde{V}^{+}_{\tilde{m}_{\tilde{j}}}$ the left and right states of the front $\tilde{f}_{\tilde{m}_{\tilde{j}}}$ of the piecewise constant wave solution $\widetilde{V}_{\tilde{m}}(x)$, respectively. In the approximation of continuous phenomena the linearization should also result in a continuous function by defining

$$\widetilde{W}_{\tilde{m}_{\tilde{j}}} = \widetilde{W}^{-}_{\tilde{m}_{\tilde{j}}} = \widetilde{W}^{+}_{\tilde{m}_{\tilde{j}}}, \tag{23}$$

if $\tilde{f}_{\text{type}_{\tilde{m}_{\tilde{j}}}} \in \{\text{lch}, \text{ich}, \text{rch}, \text{lcw}, \text{icw}, \text{rcw}\}$, where $\widetilde{W}_{\tilde{m}_{\tilde{j}}}$ is the value of the piecewise linear wave solution $\widetilde{W}_{\tilde{m}}(x)$ at front $\tilde{f}_{\tilde{m}_{\tilde{j}}}$. The actual flow conditions at the fronts representing continuous phenomena are given by the left neighboring state for leftmost characteristics and contact waves

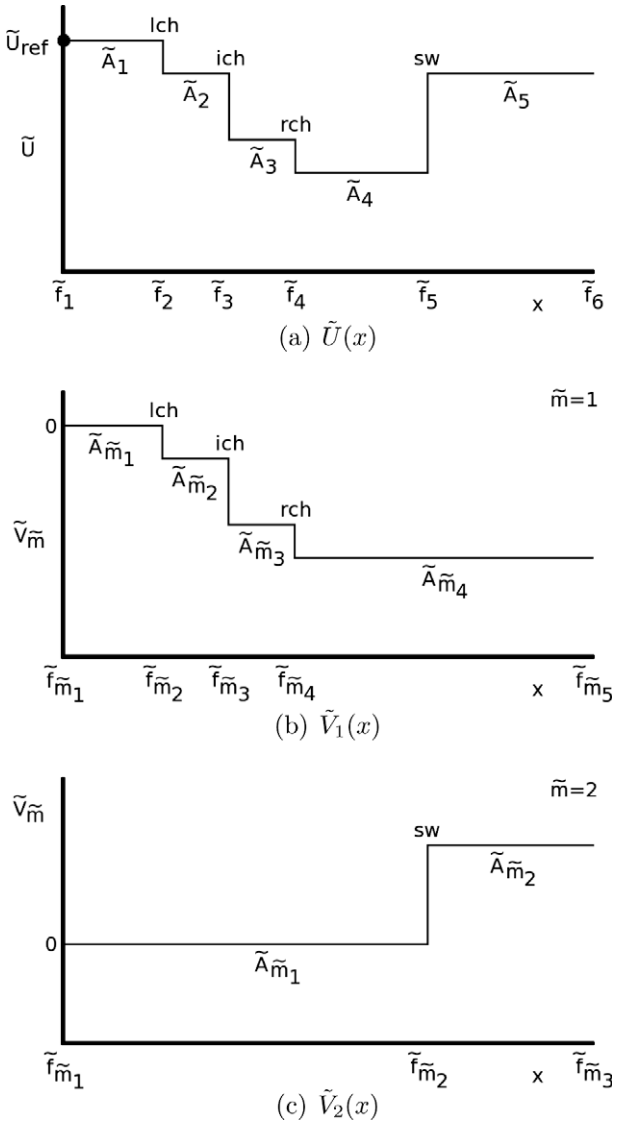

(a) $\tilde{U}(x)$

(b) $\tilde{V}_1(x)$

(c) $\tilde{V}_2(x)$

Fig. 5. Wave decomposition.

$$\widetilde{W}_{\tilde{m}_j} = \widetilde{V}^{-}_{\tilde{m}_j}, \tag{24}$$

for $\tilde{f}_{\text{type}_{\tilde{m}_j}} \in \{\text{lch}, \text{lcw}\}$, and equivalently for rightmost characteristics and contact waves

$$\widetilde{W}_{\tilde{m}_j} = \widetilde{V}^{+}_{\tilde{m}_j}, \tag{25}$$

for $\tilde{f}_{\text{type}_{\tilde{m}_j}} \in \{\text{rch}, \text{rcw}\}$. The linearization at internal characteristics and contact waves is given by the arithmetic average of the left and right neighboring states

$$\widetilde{W}_{\tilde{m}_j} = \frac{\widetilde{V}^{-}_{\tilde{m}_j} + \widetilde{V}^{+}_{\tilde{m}_j}}{2}, \tag{26}$$

for $\tilde{f}_{\text{type}_{\tilde{m}_j}} \in \{\text{ich}, \text{icw}\}$. By combining (22)–(26) the left and right states at the fronts $\tilde{f}_{\tilde{m}_j}$ after the linearization can be summarized as

$$\widetilde{W}^{-}_{\tilde{m}_j} = \begin{cases} \widetilde{V}^{-}_{\tilde{m}_j}, & \tilde{f}_{\text{type}_{\tilde{m}_j}} \in \{\text{sw}, \text{cd}, \text{lch}, \text{lcw}\}, \\ \widetilde{V}^{+}_{\tilde{m}_j}, & \tilde{f}_{\text{type}_{\tilde{m}_j}} \in \{\text{rch}, \text{rcw}\}, \\ \frac{1}{2}(\widetilde{V}^{-}_{\tilde{m}_j} + \widetilde{V}^{+}_{\tilde{m}_j}), & \tilde{f}_{\text{type}_{\tilde{m}_j}} \in \{\text{ich}, \text{icw}\}, \end{cases} \tag{27}$$

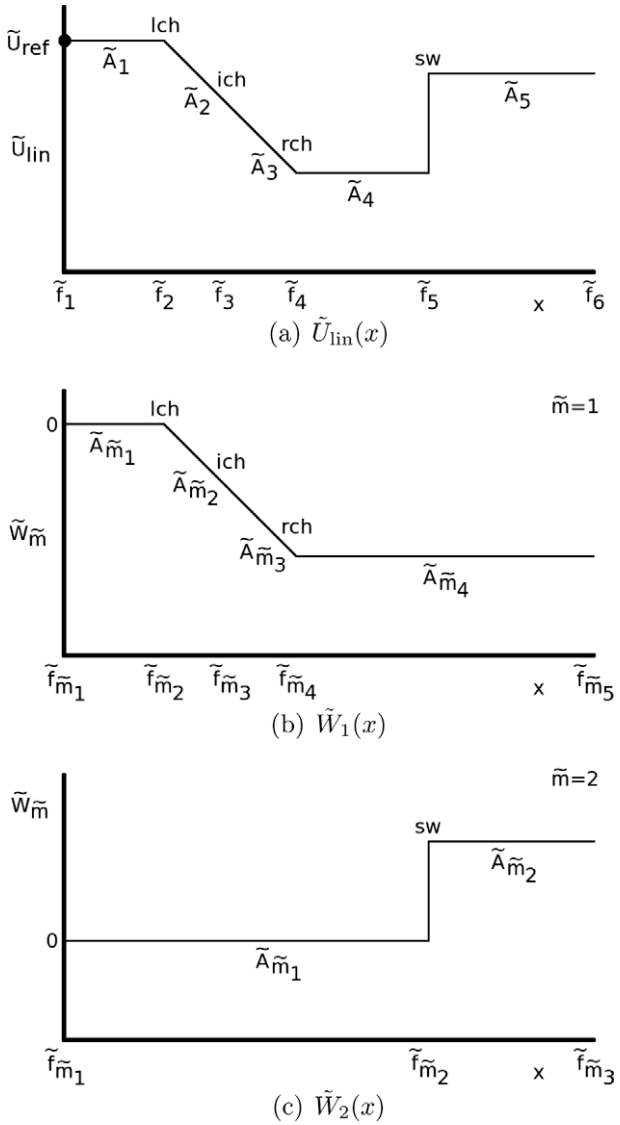

Fig. 6. Linearization.

and

$$\widetilde{W}^{+}_{\tilde{m}_j} = \begin{cases} \widetilde{V}^{-}_{\tilde{m}_j}, & \tilde{f}_{\mathrm{type}_{\tilde{m}_j}} \in \{\mathrm{lch}, \mathrm{lcw}\}, \\ \widetilde{V}^{+}_{\tilde{m}_j}, & \tilde{f}_{\mathrm{type}_{\tilde{m}_j}} \in \{\mathrm{sw}, \mathrm{cd}, \mathrm{rch}, \mathrm{rcw}\}, \\ \frac{1}{2}(\widetilde{V}^{-}_{\tilde{m}_j} + \widetilde{V}^{+}_{\tilde{m}_j}), & \tilde{f}_{\mathrm{type}_{\tilde{m}_j}} \in \{\mathrm{ich}, \mathrm{icw}\}. \end{cases} \tag{28}$$

In addition all wave solutions $\widetilde{V}_{\tilde{m}}(x)$ are enriched by nodes at locations of discontinuities in the other wave solutions to allow for discontinuous changes of the spatial derivative of flow conditions in, for example, a rarefaction fan in interaction with a shock wave or contact discontinuity. The left and right state at these additional nodes are determined by linear extrapolation of the linearized left and right states $\widetilde{W}_{\tilde{m}}(x)$, respectively. The values at the boundaries of the spatial domain are also found by linear extrapolation from the interior.

The piecewise linear reconstruction of the front tracking solution $\widetilde{U}_{\mathrm{lin}}(x)$ is finally obtained by summing the linearized wave solutions $\widetilde{W}_{\tilde{m}}(x)$ in an inverse of the wave decomposition step (18)

$$\widetilde{U}_{\mathrm{lin}}(x) = \widetilde{U}_{\mathrm{ref}} + \sum_{\tilde{m}=1}^{\tilde{n}_{\mathrm{wave}}} \widetilde{W}_{\tilde{m}}(x), \tag{29}$$

see Fig. 6(a).

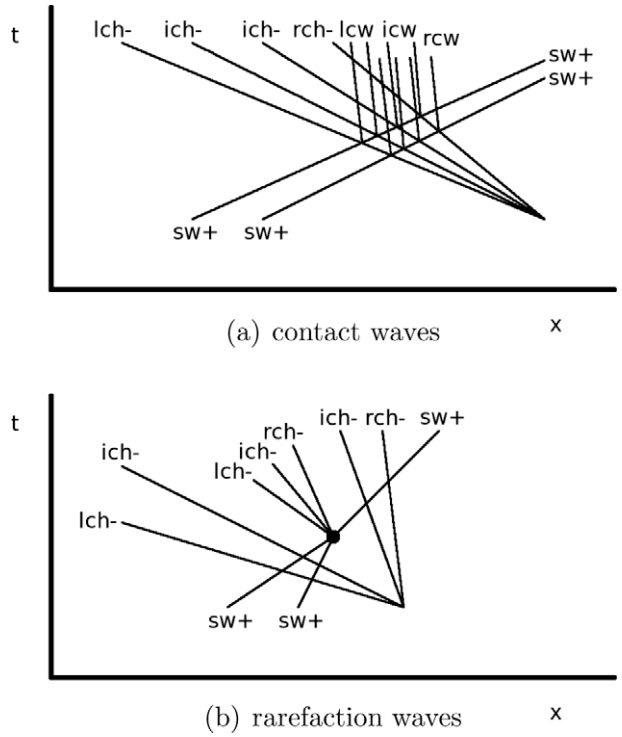

Fig. 7. Complex wave interactions with coinciding waves of the same family.

3.4. Piecewise linear front tracking algorithm

The algorithm for computing the piecewise linear front tracking solution of the Euler equations can be summarized as follows:

1. Find the piecewise constant front tracking solution using the improved front tracking method with the additional tracking and interaction modeling of the front numbers f_{number_j} as given by front number interaction model h_l (14) and tabulated in d_l (17);
2. Decompose the piecewise constant front tracking solution $\widetilde{U}(x)$ at $t = \tilde{t}$ into its wave solutions $\widetilde{V}_{\tilde{m}}(x)$ for $\tilde{m} = 1, \ldots, \tilde{n}_{\text{wave}}$ using (18);
3. Linearize the wave solutions $\widetilde{V}_{\tilde{m}}(x)$ separately to $\widetilde{W}_{\tilde{m}}(x)$ by taking the front types $\tilde{f}_{\text{type}_{\tilde{m}_j}}$ into account according to (27) and (28);
4. Construct the piecewise linear front tracking solution $\widetilde{U}_{\text{lin}}(x)$ by summing the linearized wave solutions $\widetilde{W}_{\tilde{m}}(x)$ as given by (29);

In order to construct the piecewise linear solution at multiple time levels, steps 2–4 can be repeated for different $t = \tilde{t}$. The piecewise linear reconstruction is able to achieve second order convergence, since the piecewise constant front tracking method predicts the front locations with second order accuracy. Decomposing the front tracking solution into wave solutions instead of only wave families is essential to apply the linearization algorithm in complex situations where multiple waves of the same family coincide. An example of two overlapping contact waves is given in Fig. 7(a) as caused by two right running shock waves crossing a left running centered rarefaction fan. A wave decomposition is necessary in this case for a consistent linearization of the contact waves. Another example is shown in Fig. 7(b) for two temporarily coinciding left running rarefaction waves caused by an intersection of two right running shock waves in a pre-existing left running rarefaction wave. A number of fronts which are not essential for the example is omitted here for clarity of the figure.

4. Sod's Riemann problem

The convergence behavior of the piecewise linear front tracking method is numerically studied first for Sod's Riemann problem as a standard test problem for the Euler equations in one spatial dimension on an infinite spatial domain in Section 4.1 and in a closed shock tube in Section 4.2.

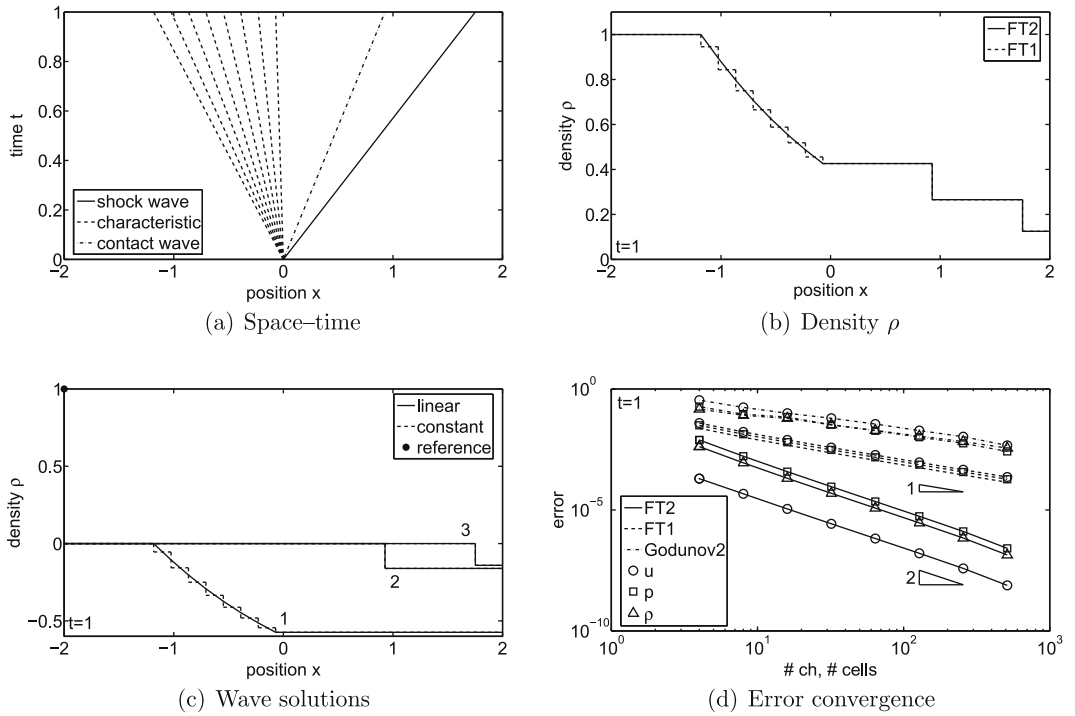

(a) Space–time (b) Density ρ

(c) Wave solutions (d) Error convergence

Fig. 8. Sod's Riemann problem on an infinite spatial domain for the piecewise linear (FT2) and piecewise constant (FT1) front tracking methods, and the second order Godunov method (Godunov2).

4.1. Infinite spatial domain

The initial condition of Sod's Riemann problem consists of two constant states separated by a discontinuity at $x = 0$. The infinite spatial domain can be treated in the front tracking method by using two infinite cells left and right of the leftmost and rightmost front, respectively. The infinite domain can also be truncated at locations far enough from $x = 0$ such that the boundaries do not cause wave reflections. The left and right state are given by [26]

$$\begin{cases} u^- = 0, \\ p^- = 1, \\ \rho^- = 1, \end{cases} \qquad \begin{cases} u^+ = 0, \\ p^+ = 0.1, \\ \rho^+ = 0.125. \end{cases} \tag{30}$$

The evolution of the front tracking solution in space–time is shown in Fig. 8(a) up to $t = 1$. The flow solution consists of a left running centered rarefaction wave discretized using $n_f = 8$ characteristic fronts, a right running shock wave, and a contact discontinuity which separates the left and right post-states. The resulting approximation for the piecewise linear and piecewise constant front tracking methods at $t = 1$ is considered in Fig. 8(b) for the density ρ to visualize also the contact discontinuity. The other primary flow quantities give rise to the same observations. Both approaches resolve the shock wave and contact discontinuity as a true discontinuity. The two results differ in the approximation of the continuous variation of the flow conditions in the rarefaction wave. The piecewise linear solution leads to a continuous representation of the rarefaction wave in contrast to the staircase behavior resulting from the piecewise constant method.

The piecewise linear solution is constructed by first decomposing the piecewise constant solution into the three wave solutions $\widetilde{V}_{\tilde{m}}(x)$ and reference value $\widetilde{U}_{\text{ref}}$ as shown in Fig. 8(c). The reference density is equal to its left most value of $\tilde{\rho}_{\text{ref}} = 1$. The solution is decomposed by grouping the fronts $\tilde{f}_{\tilde{m}_j}$ with wave numbers $\tilde{v}_{\text{number}_{\tilde{m}}}$ of the: (1) rarefaction wave; (2) contact discontinuity; and (3) shock wave. The corresponding front types $\tilde{f}_{\text{type}_{\tilde{m}_j}}$ are used in the linearization procedure where the discontinuous phenomena are unaffected. The density in the rarefaction wave is linearized by averaging the left and right value at the location of an internal characteristic. At the leftmost and rightmost characteristic the left and right state is adopted, respectively.

The error convergence for the velocity u, pressure p, and density ρ at $t = 1$ with respect to a fine reference solution in Fig. 8(d) demonstrates that the piecewise linear reconstruction leads for this problem to a second order error convergence rate as function of the number of characteristics n_f discretizing the rarefaction wave. The employed L_1 error measure is defined as

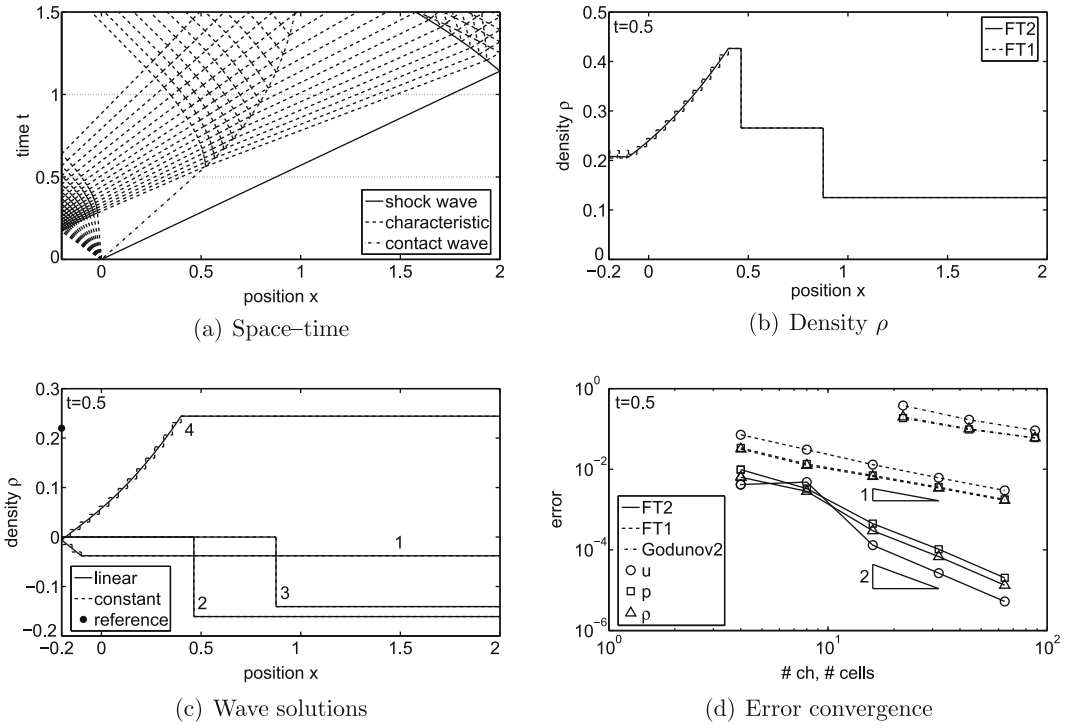

(a) Space–time (b) Density ρ

(c) Wave solutions (d) Error convergence

Fig. 9. Sod's Riemann problem in a closed shock tube for the piecewise linear (FT2) and piecewise constant (FT1) front tracking methods, and the second order Godunov method (Godunov2) at $t = 0.5$.

$$\varepsilon_{L_1}(t) = \frac{\|z(x,t) - z_{\text{fine}}(x,t)\|_1}{\|z_{\text{fine}}(x,t)\|_1}, \tag{31}$$

with $z = \{u, p, \rho\}$. The second order convergence results in an up to four orders of magnitude smaller error than the first order piecewise constant front tracking method. For comparison also results for the second order Godunov method [29] based on an algebraic average flux limiter are shown as function of the number of spatial volumes in the finite volume discretization. For the Godunov method the infinite spatial domain is truncated to $x \in [-2, 2]$ such that the wave phenomena do not reach the boundaries for $t \leqslant 1$. The result that the actual Godunov convergence rate reduces for this discontinuous solution as anticipated to first order verifies the validity of the reference solution. The resulting error is also an order of magnitude larger than for the first order front tracking method. This reflects the efficient discretization of the space–time domain achieved by the front tracking algorithm. More advanced second order finite volume discretizations are beyond the scope of this work, since the comparison is here intended for verification only.

4.2. Closed shock tube

A more challenging problem for front tracking methods involving front interactions is obtained by limiting the spatial domain of Sod's Riemann problem to a closed shock tube. In this section the initial conditions (30) are considered on the domain

$$x \in [-0.2; 2], \tag{32}$$

with reflective boundaries at $x = -0.2$ and $x = 2$. At a front interaction with a boundary a piston problem is solved in an analogous way to how a Riemann problem is used to resolve an interaction of two fronts. The space–time front tracking solution with $n_f = 16$ fronts in the rarefaction wave discretization is shown in Fig. 9(a) up to $t = 1.5$. The left running rarefaction wave reflects on the left boundary before it interacts with the contact discontinuity and the shock wave reflected from the right boundary at $x = 2$. The solution is considered at the time levels $t = \{0.5; 1; 1.5\}$ denoted by the horizontal dotted lines.

At $t = 0.5$ the rarefaction wave is reflecting from the left boundary, which leads to an interaction of the incident and reflected wave. This results in relatively small density gradients in the interaction region close to the wall for $x \in [-0.2; -0.1]$ in Fig. 9(b). The piecewise constant front tracking method gives in this region a tooth-shaped approximation due to the interaction of the two waves, see Fig. 10 for an enlarged view. The piecewise linear approach gives a continuous solution in both the reflected rarefaction wave and the interaction region. This is achieved by the automatic introduction of a fourth wave number for the reflected wave in the decomposition of Fig. 9(c). The incident and reflected rarefaction wave are then

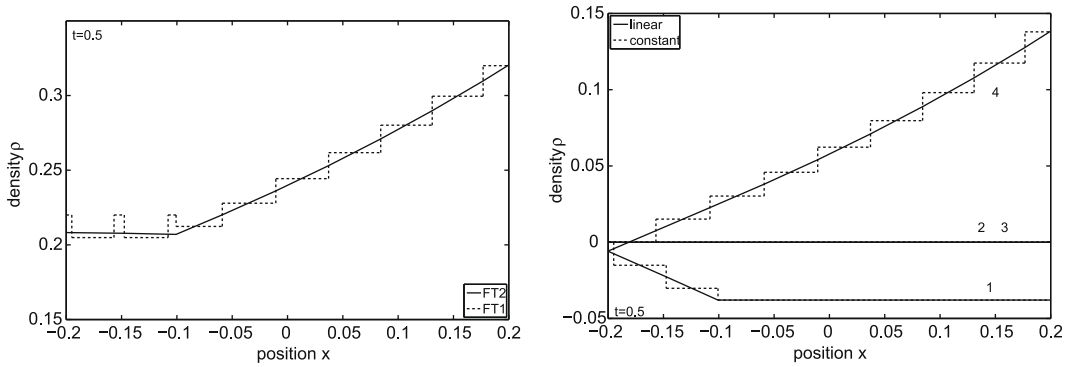

(a) Density ρ (b) Wave solutions

Fig. 10. Zoom of Sod's Riemann problem in a closed shock tube for the piecewise linear (FT2) and piecewise constant (FT1) front tracking methods at $t = 0.5$.

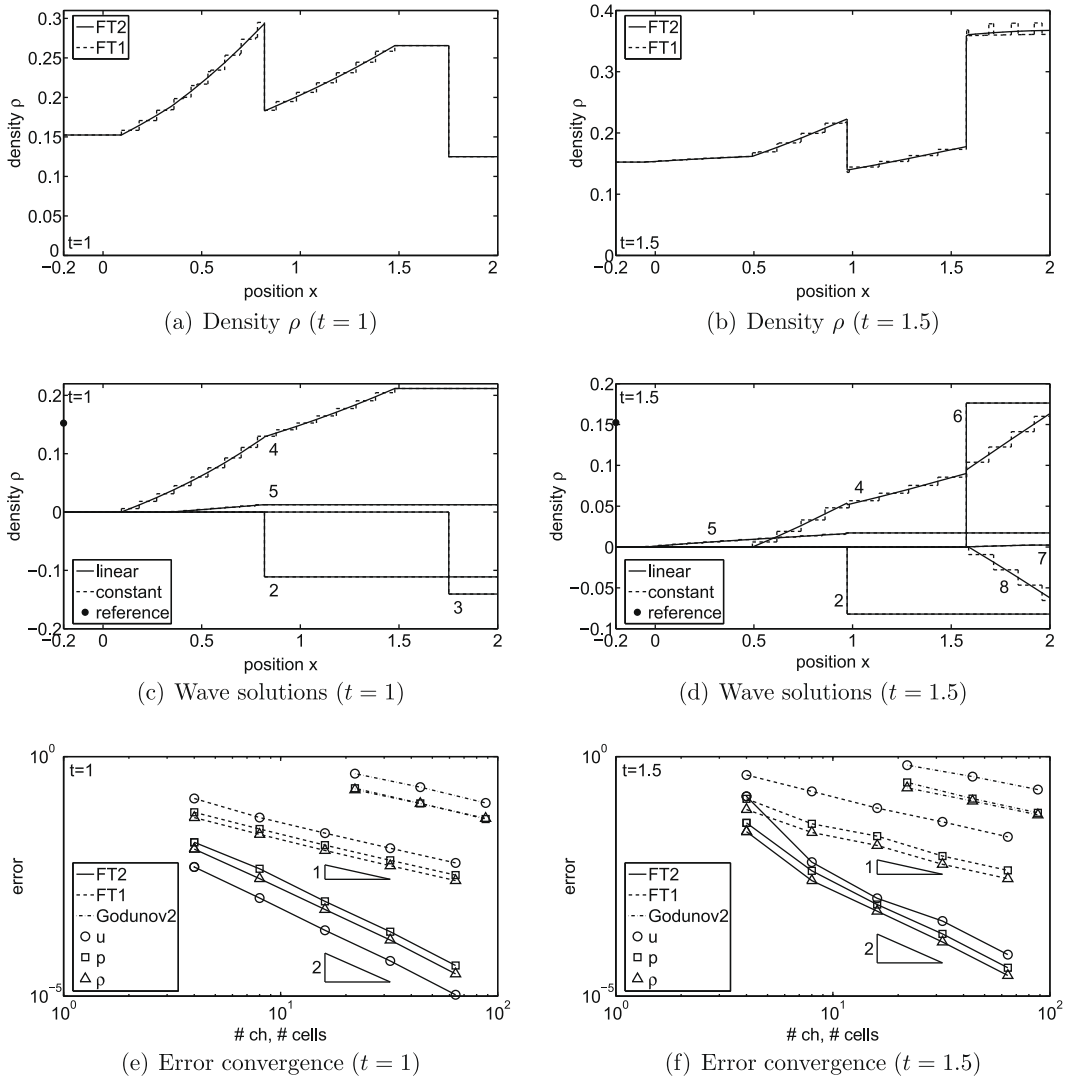

(a) Density ρ $(t = 1)$ (b) Density ρ $(t = 1.5)$

(c) Wave solutions $(t = 1)$ (d) Wave solutions $(t = 1.5)$

(e) Error convergence $(t = 1)$ (f) Error convergence $(t = 1.5)$

Fig. 11. Sod's Riemann problem in a closed shock tube for the piecewise linear (FT2) and piecewise constant (FT1) front tracking methods, and the second order Godunov method (Godunov2) at $t = 1$ and $t = 1.5$.

linearized independently. The piecewise linear front tracking method maintains a second order convergence rate in the wave interaction region as shown in Fig. 9(d).

The interaction of right running rarefaction wave number 4 with the contact discontinuity at $t = 1$ shown in Fig. 11(a) results in the creation of a reflected left running fan of characteristics, which is an isentropic compression wave. The discretization of this reflection leads to a new wave number 5 in the wave solution decomposition of Fig. 11(c). Wave number 1 is no longer present in the decomposition, since the reflection of the initial left running rarefaction wave onto the left boundary has been completed before $t = 1$. At $t = 1.5$ the right running rarefaction wave 4 is reflecting from the right boundary and also interacting with the reflected shock wave. The continuous change of entropy at the right of the curved shock wave path in the shock wave/rarefaction interaction region is discretized using a series of contact waves. These phenomena are resolved by three additional wave numbers, see Fig. 11(b) and (d). Also for these increasingly complex wave interactions, piecewise linear front tracking remains second order accurate in Fig. 11(e) and (f). It is observed that the error increases slightly with time for a fixed number of fronts per rarefaction wave, which is an intrinsic property of the front tracking method [17] and caused by the increasing detail in the solution.

5. Two interacting blast waves problem

A classical test problem for assessing the performance of numerical methods in the presents of strong discontinuities is the two interacting blast waves problem introduced by Woodward [32]. The blast waves shock tube problem on the domain $x = [0, 1]$ is defined by the initial condition consisting of three uniform regions for the pressure

$$p = \begin{cases} 1000, & 0 < x < 0.1, \\ 0.01, & 0.1 < x < 0.9, \\ 100, & 0.9 < x < 1, \end{cases} \tag{33}$$

and constant velocity $u = 0$ and density $\rho = 1$ between reflecting walls at $x = 0$ and $x = 1$. The solution until $t = 0.04$ involves the interaction of the strong shock waves and contact discontinuities with the reflections of the rarefaction waves created at the jumps in the initial condition. This results in a highly complex interaction in the collision region as illustrated by the space–time front tracking solution for a discretization of the rarefaction waves with $\delta = 0.1$ in Fig. 12(a). The piecewise linear front tracking solution of the density ρ, velocity u, and pressure p at $t = 0.038$ for $\delta = 0.05$ of Fig. 12(b) to (d) gives a smooth approximation of the continuous regions and a sharp resolution of the discontinuities. The detailed flow features in the collision region clearly visible in the density profile around $x = 0.8$ affect the velocity and pressure to a lesser extend. The predicted flow field shows excellent agreement with the benchmark results presented in [33].

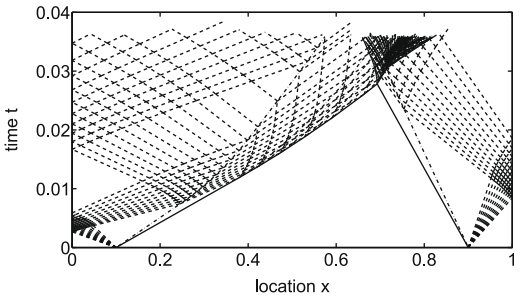

The time evolution of the density ρ between $t = 0$ and $t = 0.038$ at times also considered in literature [33] is given in Fig. 13. Initially for $t \leqslant 0.026$ the density shows that the two sets of strong waves emanating from the left and right discontinuity in the initial conditions reflect on the boundaries and interact with each other separately resulting in a maximum density of $\rho = 6.0$. After the intersection of the two shock waves the density peaks at $\rho = 28.52$ for $t = 0.028$ and decreases with increasing time.

The error convergence for u, p, and ρ of piecewise linear front tracking is compared in Fig. 14 to that of piecewise constant front tracking as function of δ. The results show that the piecewise linear approximation achieves second order convergence also in case of strong waves and their interactions for $t \leqslant 0.026$. In the collision region for $t \geqslant 0.028$ the method converges to second order accuracy at lower values of δ due to the high level of detail in solution. The piecewise linear front tracking method consistently achieves higher convergence rates and significantly lower errors than the first order piecewise constant front tracking method.

6. Two-dimensional supersonic airfoil flow

The meshless front tracking method is also an effective approach for simulating two-dimensional supersonic steady Euler flows. In that case the free stream flow direction instead of the time axis is treated as the hyperbolic coordinate. This approach is applicable if the velocity component in the direction of the undisturbed flow streamlines is supersonic throughout the whole flow field. This implies, for example, an airfoil flow with attached shock waves at the sharp leading and trailing

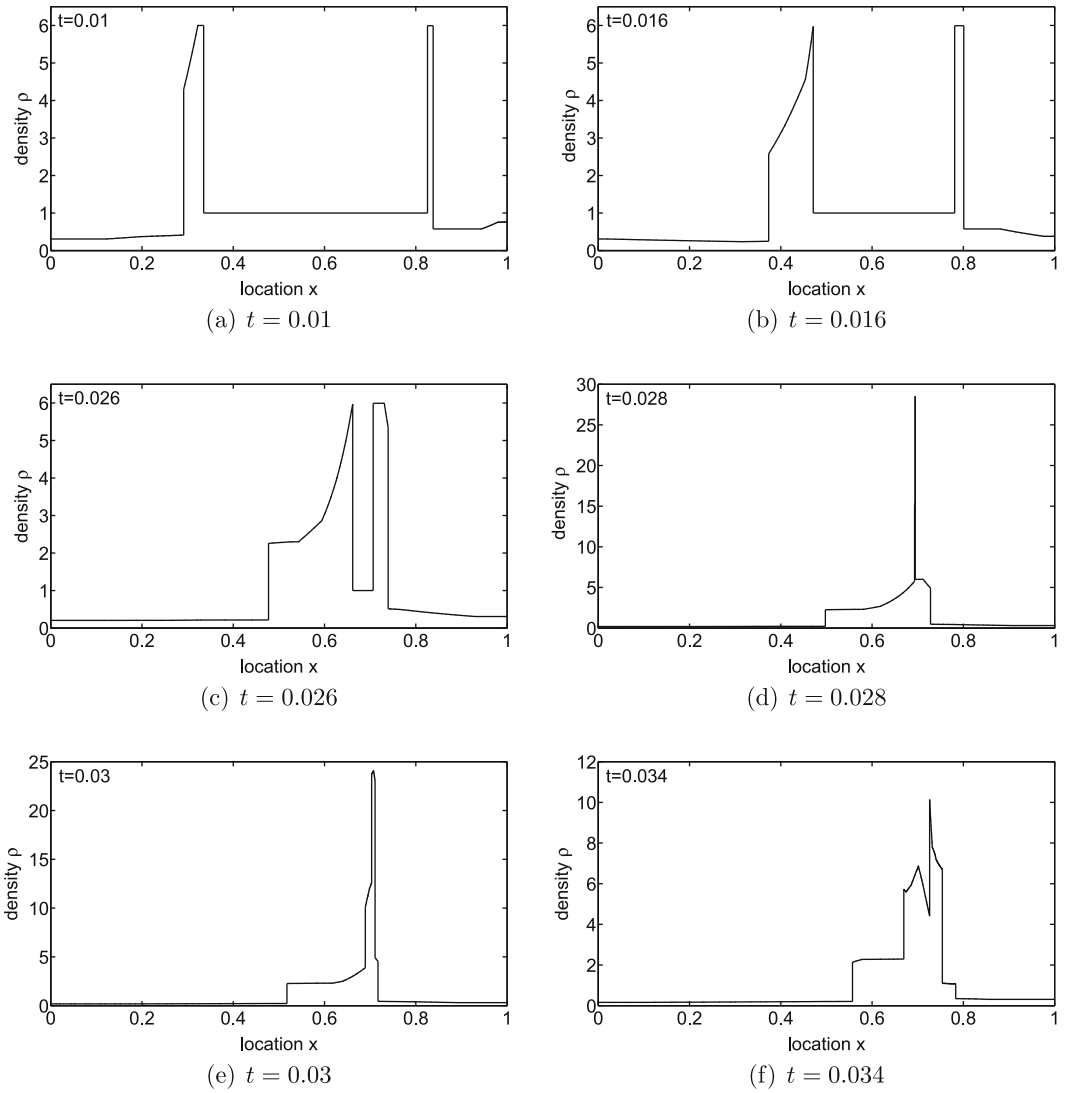

Fig. 13. Density of the two interacting blast waves problem from $t = 0.01$ to $t = 0.034$ for $\delta = 0.05$.

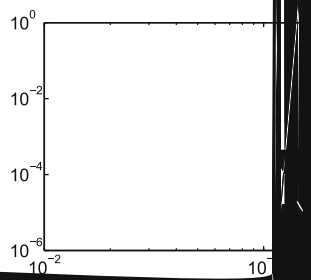

$$= 0,$$

$$F = \begin{pmatrix} \rho u \\ \rho u^2 + p \\ \rho u v \\ \rho u H \end{pmatrix},$$

The front tracking algorithm
tional unknown v is stored
supersonic equivalents. The

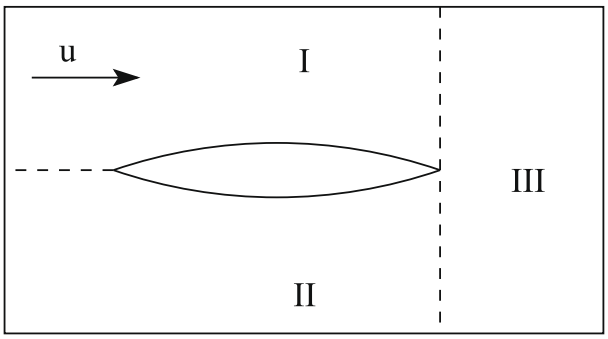

Fig. 15. Spatial domain decomposition for the two-dimensional supersonic airfoil flow.

The considered geometry is a symmetrical circular-arc airfoil with chord length $c = 0.1$ m, 12% thickness, and a leading and trailing edge semi-opening angle of $\theta_0 = 13.69°$. In order to solve the airfoil flow problem for non-zero angle of attack the flow domain is divided into three subdomains shown in Fig. 15. The three domains are separated by a horizontal line from the leading edge pointing in the upstream direction and a vertical line through the trailing edge. The flow in domains *I* and *II* can be resolved independently from each other and potentially in parallel due to the hyperbolicity of the problem. The solutions of *I* and *II* at the *x*-coordinate of the trailing edge are used as boundary condition for domain *III*, which contains the trailing edge shocks and the inviscid entropy wake behind the airfoil. For computing the aerodynamic forces on the airfoil using surface pressure integration it is sufficient to consider domains *I* and *II* only.

The flow solutions for two cases with different free stream Mach numbers $M_\infty = 2$ and $M_\infty = 2.5$ and angle of attack $\alpha = 5°$ are given in Fig. 16 in terms of the Mach number field and the computational grid for a discretization of the airfoil with 40 points at each side. The piecewise linear front tracking results show a sharp resolution of the curved leading and trailing edge shock waves also farther away from the airfoil. This property makes the method particularly useful for resolving the flow features in the far field. The case for $M_\infty = 2.5$ results in sharper shock wave angles with respect to the free stream flow direction and a larger range of Mach numbers in the flow field. Fig. 16(c) and (d) illustrate the highly efficient discretization of the spatial flow domain with only two cells for representing the undisturbed flow upstream of the leading edge shock waves. The curvature of the shock waves is resolved by the interaction of the shock waves with the rarefaction

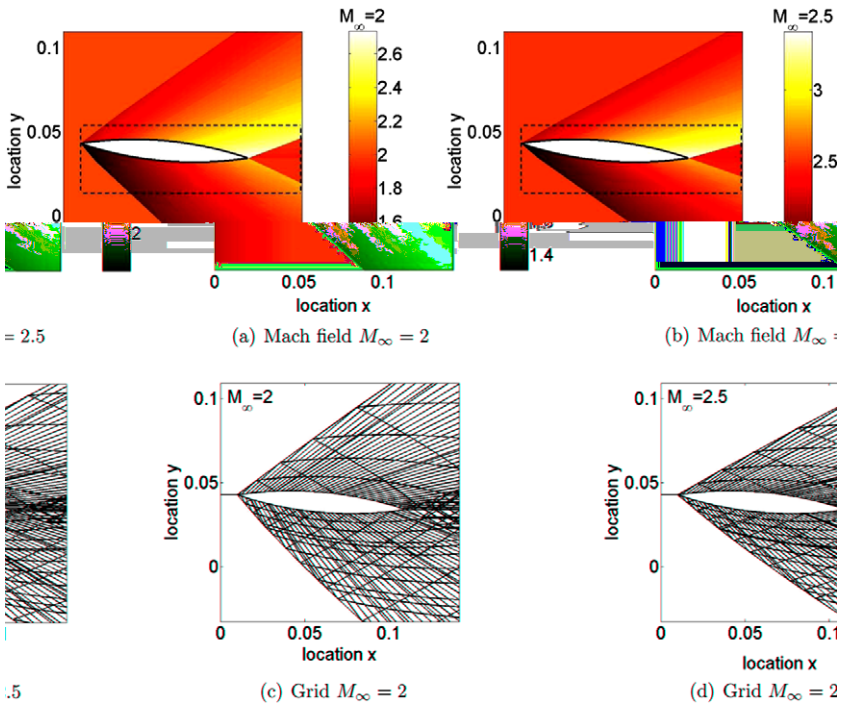

Fig. 16. Mach field and grid for the two-dimensional supersonic airfoil flow.

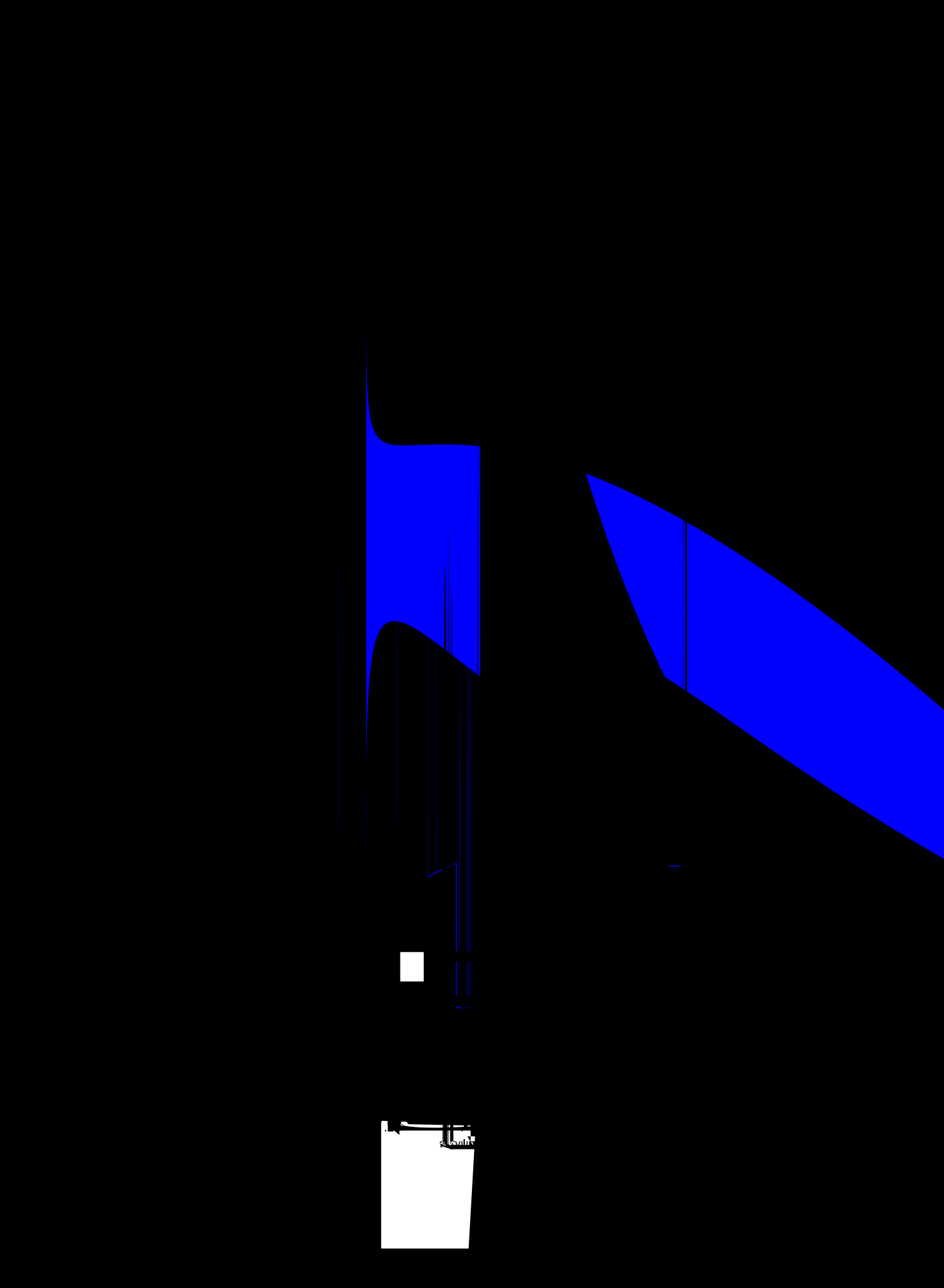

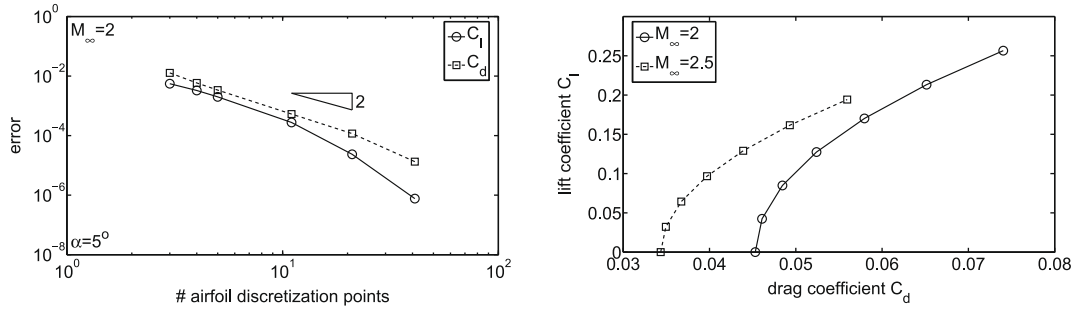

(a) Error convergence (b) Lift–drag curve

Fig. 19. Lift and drag coefficients for the two-dimensional supersonic airfoil flow.

of the curvilinear abscissa normalized by the airfoil chord s/c. The dotted vertical lines indicate the location of the corners of the integration contour. The velocity components predicted by the front tracking solution of the Euler equations closely agree with the experimental data, which indicates that viscous effects are generally small in this flow problem. The numerical and experimental results also show the same trends for the velocity components as function of the Mach number. The numerical solution shows clearly the inviscid entropy wake behind the airfoil for the streamwise velocity component u, see the enlarged view in Fig. 18 for $M_\infty = 2$. The entropy wake is largest behind the upper surface due to the high pre-shock Mach number in combination with the relatively high curvature of the trailing edge shock wave. The slip line emanating from the trailing edge of the airfoil is also resolved as a true discontinuity. In the experimental results the local effect of the viscous wake can be recognized. Numerical results for the other flow conditions show a constant pressure over the slip line, and small discontinuities in the density and temperature.

Finally the lift-drag curve of the airfoil for angles of attack between $\alpha = 0^\circ$ and $\alpha = 6^\circ$ is considered in Fig. 19 based on pressure integration over the airfoil surface in terms of the lift and drag coefficients

$$C_l = \frac{L}{\frac{1}{2}\rho_\infty u_\infty^2 c}, \tag{36}$$

$$C_d = \frac{D}{\frac{1}{2}\rho_\infty u_\infty^2 c}, \tag{37}$$

with lift and drag forces L and D, and coefficients C_l and C_d, respectively. As an illustration the second order convergence of C_l and C_d for $M_\infty = 2$ and $\alpha = 5^\circ$ is given in Fig. 19(a) for an increasing number of airfoil surface discretization points. The lift-drag curve of Fig. 19(b) shows the typical parabolic trend with lower lift and drag coefficients for the higher Mach number of $M_\infty = 2.5$ in the considered range of angles of attack.

7. Conclusions

A second order front tracking method for the Euler equations is developed based on a piecewise linear reconstruction of the piecewise constant front tracking solution. The piecewise linear solution is obtained by first decomposing the front tracking approximation into wave solutions. The wave components are then linearized separately based on the physical phenomena of the fronts as tracked by the front types of the improved front interaction model. For the wave decomposition also front numbers are tracked to denote the wave to which the fronts belong. The front interaction model is extended to resolve the interaction of the front numbers at front intersections.

Second order convergence results for Sod's Riemann problem lead to an up to four orders of magnitude smaller error than the first order piecewise constant front tracking method. After truncation of the spatial domain to a closed shock tube the method maintains second order convergence in the presence of front interactions and reflections. A comparison with a second order Godunov finite volume method verifies the consistency of the developed approach. The solution of the two interacting blast waves problem shows a sharp resolution of discontinuities and a smooth approximation of continuous flow regions. An error convergence study shows that the piecewise linear front tracking method also converges to second order accuracy for the interaction of strong waves.

The validation study for a two-dimensional supersonic airfoil flow over a range of angles of attack up to $\alpha = 6^\circ$ and for Mach numbers $M_\infty = 2$ and $M_\infty = 2.5$ shows a good agreement with the experimental PIV data. The resulting computational grids illustrate the highly efficient discretization of the spatial flow domain by the front tracking method. The predicted lift and drag coefficients in the lift-drag diagram also show a second order convergence rate.

Interesting directions for further research include the mathematical proof of the second order accuracy and the extension to higher order convergence rates involving continuously varying front velocities. The second order front tracking method has been developed here for one-dimensional unsteady and two-dimensional supersonic flows. Extensions to

higher-dimensional unsteady problems will be considered in future work by employing the dimensional splitting technique. The front tracking algorithm and the piecewise linear reconstruction are then applied to each spatial coordinate independently on a Cartesian mesh. The flow in the different spatial directions is in that case coupled in the spatial volumes of the multi-dimensional mesh.

Acknowledgments

The author would like to acknowledge Louis Souverein, Bas van Oudheusden, and Fulvio Scarano for providing the experimental PIV velocity measurements in the collaborative validation study for the two-dimensional supersonic airfoil flow problem. Barry Koren is also acknowledged for his suggestions regarding the second order Godunov finite volume scheme.

Appendix A. Front number interaction model

In this appendix the front interaction model for the front numbers is introduced that prescribes the wave numbers w_{number_l} of the created waves at a front intersection as function of the front types, front families, and front numbers of the intersecting fronts. The wave number w_{number_l} can be equal to the front number of one of the intersecting fronts or a new wave number.

In Tables 1–3 the front number interaction model h_l is given for $l = \{\text{left}, \text{middle}, \text{right}\}$. The front type f_{type_j} and family f_{family_j} of the intersecting left and right front, j_{left} and j_{right}, are shown vertically and horizontally, respectively. A front type f_{type_j} can be a shock wave (sw), left/internal/right characteristic of a fan of characteristics (lch/ich/rch), contact discontinuity (cd), or left/internal/right contact wave of a continuous change in entropy (lcw/icw/rcw). The front families f_{family_j} are left running (−), right running (+), and waves with no relative velocity with respect to the local fluid (0).

The predicted wave number w_{number_l} is given by an "l" or "r", if w_{number_l} is equal to the front number f_{number_j} of the left or right intersecting front, j_{left} or j_{right}, respectively. An "n" denotes that the created wave w_l has a new wave number. Not all front intersections of Tables 1–3 can occur in practice. For example, two fronts of family (0) with no relative velocity with respect to the surrounding fluid cannot intersect. These physically impossible front intersections are given by a "×". The prescribed wave number w_{number_l} is then assigned to the created waves according to (14). The front numbers are derived from w_{number_l} as given by (16).

Table 1
Front number interaction model h_l for the left created wave $l = \text{left}$.

Type	Right	sw	sw	lch	lch	rch	rch	ich	ich	cd	lcw	rcw	icw
Left	Fam.	−	+	−	+	−	+	−	+	0	0	0	0
sw	−	n	×	l	×	l	×	l	×	×	×	×	×
sw	+	r	n	r	n	r	n	r	n	n	n	n	n
lch	−	r	×	×	×	n	×	n	×	×	×	×	×
lch	+	r	n	r	×	r	n	r	n	n	n	n	n
rch	−	r	×	×	×	×	×	×	×	×	×	×	×
rch	+	r	n	r	×	r	×	r	×	n	n	n	n
ich	−	r	×	×	×	n	×	n	×	×	×	×	×
ich	+	r	n	r	×	r	n	r	n	n	n	n	n
cd	0	r	×	r	×	r	×	r	×	×	×	×	×
lcw	0	r	×	r	×	r	×	r	×	×	×	×	×
rcw	0	r	×	r	×	r	×	r	×	×	×	×	×
icw	0	r	×	r	×	r	×	r	×	×	×	×	×

Table 2
Front number interaction model h_l for the middle created wave $l = \text{middle}$.

Type	Right	sw	sw	lch	lch	rch	rch	ich	ich	cd	lcw	rcw	icw
Left	Fam.	−	+	−	+	−	+	−	+	0	0	0	0
sw	−	n	×	n	×	n	×	n	×	×	×	×	×
sw	+	n	n	n	n	n	n	n	n	r	r	r	r
lch	−	n	×	×	×	n	×	n	×	×	×	×	×
lch	+	n	n	×	×	×	n	×	n	r	r	r	r
rch	−	n	×	×	×	×	×	×	×	×	×	×	×
rch	+	n	n	×	×	×	×	×	×	r	r	r	r
ich	−	n	×	×	×	n	×	n	×	×	×	×	×
ich	+	n	n	×	×	×	n	×	n	r	r	r	r
cd	0	l	×	l	×	l	×	l	×	×	×	×	×
lcw	0	l	×	l	×	l	×	l	×	×	×	×	×
rcw	0	l	×	l	×	l	×	l	×	×	×	×	×
icw	0	l	×	l	×	l	×	l	×	×	×	×	×

Table 3
Front number interaction model h_l for the right created wave l = right.

Type Left	Right Fam.	sw −	sw +	lch −	lch +	rch −	rch +	ich −	ich +	cd 0	lcw 0	rcw 0	icw 0
sw	−	n	×	n	×	n	×	n	×	×	×	×	×
sw	+	l	n	l	l	l	l	l	l	l	l	l	l
lch	−	n	×	×	×	n	×	n	×	×	×	×	×
lch	+	l	r	l	×	l	n	l	n	l	l	l	l
rch	−	n	×	×	×	×	×	×	×	×	×	×	×
rch	+	l	r	l	×	l	×	l	×	l	l	l	l
ich	−	n	×	×	×	n	×	n	×	×	×	×	×
ich	+	l	r	l	×	l	n	l	n	l	l	l	l
cd	0	n	×	n	×	n	×	n	×	×	×	×	×
lcw	0	n	×	n	×	n	×	n	×	×	×	×	×
rcw	0	n	×	n	×	n	×	n	×	×	×	×	×
icw	0	n	×	n	×	n	×	n	×	×	×	×	×

References

[1] P. Baiti, H.K. Jenssen, On the front tracking algorithm, J. Math. Anal. Appl. 217 (1998) 395–404.
[2] A. Bressan, P. LeFloch, Uniqueness of weak solution to systems of conservation laws, Arch. Rational Mech. Anal. 140 (1997) 301–317.
[3] P. Charrier, B. Tessieras, On front-tracking methods applied to hyperbolic systems of nonlinear conservation laws, SIAM J. Numer. Anal. 23 (1986) 461–472.
[4] I.-L. Chern, J. Glimm, O. McBryan, B. Plohr, S. Yaniv, Front tracking for gas dynamics, J. Comput. Phys. 62 (1986) 83–110.
[5] I.-L. Chern, P. Colella, A conservative front tracking method for hyperbolic conservation laws, Technical Report UCRL JC-97200, Lawrence Livermore National Laboratory, 1987.
[6] I.-L. Chern, Stability theorem and truncation error analysis for the Glimm scheme and for a front tracking method for flows with strong discontinuities, Commun. Pure Appl. Math. 42 (1989) 815–844.
[7] A.J. Chorin, J.E. Marsden, A Mathematical Introduction to Fluid Mechanics, Springer-Verlag, New York, 1979.
[8] G. Emanuel, Analytical Fluid Dynamics, CRC Press, Boca Raton, 2001.
[9] J. Glimm, E. Isaacson, D. Marchesin, O. McBryan, Front tracking for hyperbolic systems, Adv. Appl. Math. 2 (1981) 91–119.
[10] J. Glimm, The interaction of nonlinear hyperbolic waves, Commun. Pure Appl. Math. 41 (1988) 569–590.
[11] J. Glimm, J.W. Grove, X.L. Li, K.-M. Shyue, Y. Zeng, Q. Zhang, Three-dimensional front tracking, SIAM J. Sci. Comput. 19 (1998) 703–727.
[12] J. Glimm, X.L. Li, Y. Liu, N. Zhao, Conservative front tracking and level set algorithms, Proc. Natl. Acad. Sci. USA 25 (2001) 14198–14201.
[13] R. Holdahl, H. Holden, K.-A. Lie, Unconditionally stable splitting methods for the shallow water equations, BIT 39 (1999) 451–472.
[14] H. Holden, K.-A. Lie, N.H. Risebro, An unconditionally stable method for the Euler equations, J. Comput. Phys. 150 (1999) 76–96.
[15] H. Holden, N.H. Risebro, Front Tracking for Hyperbolic Conservation Laws, Springer-Verlag, New York, 2002.
[16] G. Moretti, Computations of flows with shocks, Ann. Rev. Fluid Mech. 19 (1987) 313–337.
[17] M. Laforest, Mechanisms for error propagation and cancellation in Glimm's scheme without rarefractions, J. Hyperbol. Differ. Eq. 4 (2007) 501–531.
[18] J.O. Langseth, N.H. Risebro, A. Tveito, A conservative front tracking scheme for 1D hyperbolic conservation laws, in: A. Donato et al. (Eds.), Nonlinear Hyperbolic Problems: Theoretical, Applied, and Computational Aspects, Notes on Numerical Fluid Mechanics, vol. 43, Vieweg, Braunschweig, 1993, pp. 385–392.
[19] K.-A. Lie, V. Haugse, K. Hvistendahl Karlsen, Dimensional splitting with front tracking and adaptive grid refinement, Numer. Meth. Part Differ. Eq. 14 (1998) 627–648.
[20] H.W. Liepmann, A. Roshko, Elements of Gasdynamics, Wiley, New York, 1957.
[21] B.J. Lucier, A moving mesh numerical method for hyperbolic conservation laws, Math. Comput. 173 (1986) 59–69.
[22] M. Raffel, C. Willert, J. Kompenhans, Particle Image Velocimetry: A Practical Guide, Springer Verlag, Berlin, 1998.
[23] R. Richtmyer, K. Morton, Difference Methods for Initial Value Problems, Interscience, New York, 1967.
[24] N.H. Risebro, A. Tveito, Front tracking applied to a nonstrictly hyperbolic system of conservation laws, SIAM J. Sci. Stat. Comput. 12 (1991) 1401–1419.
[25] N.H. Risebro, A. Tveito, A front tracking method for conservation laws in one dimension, J. Comput. Phys. 101 (1992) 130–139.
[26] G.A. Sod, A survey of several finite difference methods for systems of nonlinear hyperbolic conservation laws, J. Comput. Phys. 27 (1978) 1–31.
[27] L.J. Souverein, B.W. van Oudheusden, F. Scarano, Particle image velocimetry based loads determination in supersonic flows, in: 45th AIAA Aerospace Sciences Meeting and Exhibit, Reno, Nevada (2007) AIAA-2007-50.
[28] B.K. Swartz, B. Wendroff, AZTEC: a front tracking code based on Godunov's method, Appl. Numer. Math. 2 (1986) 385–388.
[29] E.F. Toro, Riemann Solvers and Numerical Methods for Fluid Dynamics, Springer Verlag, Berlin, 1997.
[30] J.A.S. Witteveen, A second-order front tracking method applied to the Euler equations, in: 44th AIAA Aerospace Sciences Meeting and Exhibit, Reno, Nevada (2006) AIAA-2006-1277.
[31] J.A.S. Witteveen, B. Koren, P.G. Bakker, An improved front tracking method for the Euler equations, J. Comput. Phys. 224 (2007) 712–728.
[32] P.R. Woodward, Trade-offs in designing explicit hydrodynamics schemes for vector computers, in: G. Rodrigue (Ed.), Parallel Computation, Academic Press, New York, 1982.
[33] P.R. Woodward, P. Colella, The numerical simulation of two-dimensional flow with strong shocks, J. Comput. Phys. 54 (1984) 115–173.